Waveform Tomography Reveals Channeled Flow at the Base of the Oceanic Asthenosphere

Scott French *et al.*

Science **342**, 227 (2013);
DOI: 10.1126/science.1241514

Science (print ISSN 0036-8075; online ISSN 1095-9203) is published weekly, except the last week in December, by the American Association for the Advancement of Science, 1200 New York Avenue NW, Washington, DC 20005.

12. D. Löffler *et al.*, *Phys. Rev. Lett.* **105**, 146104 (2010).
13. W. H. Zachariasen, *J. Am. Chem. Soc.* **54**, 3841–3851 (1932).
14. L. Lichtenstein, M. Heyde, H.-J. Freund, *Phys. Rev. Lett.* **109**, 106101 (2012).
15. M. Wilson, A. Kumar, D. Sherrington, M. F. Thorpe, *Phys. Rev. B* **87**, 214108 (2013).
16. F. Ben Romdhane *et al.*, *ACS Nano* **7**, 5175–5180 (2013).
17. Materials and methods are available as supplementary materials on *Science* Online.
18. Z. Lee *et al.*, *Nano Lett.* **9**, 3365–3369 (2009).
19. R. S. Pantelic, J. C. Meyer, U. Kaiser, H. Stahlberg, *Solid State Commun.* **152**, 1375–1382 (2012).
20. E. Nakamura, *Angew. Chem. Int. Ed.* **52**, 236–252 (2013).
21. A. Hashimoto, K. Suenaga, A. Gloter, K. Urita, S. Iijima, *Nature* **430**, 870–873 (2004).
22. J. C. Meyer *et al.*, *Nano Lett.* **8**, 3582–3586 (2008).
23. J. H. Warner *et al.*, *Science* **337**, 209–212 (2012).
24. J. Kotakoski *et al.*, *Phys. Rev. B* **83**, 245420 (2011).
25. J. Kotakoski, A. V. Krasheninnikov, U. Kaiser, J. C. Meyer, *Phys. Rev. Lett.* **106**, 105505 (2011).
26. S. Kurasch *et al.*, *Nano Lett.* **12**, 3168–3173 (2012).
27. S. G. Mayr, Y. Ashkenazy, K. Albe, R. S. Averback, *Phys. Rev. Lett.* **90**, 055505 (2003).
28. K. Zheng *et al.*, *Nature Communications* **1**, 24 (2010).
29. L. W. Hobbs, M. R. Pascucci, *J. Phys. Colloq.* **41**, C6-237–C6-242 (1980).
30. P. M. Ajayan, S. Iijima, *Philos. Mag. Lett.* **65**, 43–48 (1992).
31. J. C. Crocker, D. G. Grier, *J. Colloid Interface Sci.* **179**, 298–310 (1996).
32. B. A. Auld, *Acoustic Fields and Waves in Solids* (Wiley, New York, 1973).
33. S. Plimpton, *J. Comput. Phys.* **117**, 1–19 (1995).
34. E. R. Grannan, M. Randeria, J. P. Sethna, *Phys. Rev. B* **41**, 7784–7798 (1990).
35. J. M. Howe, H. Saka, *MRS Bull.* **29**, 951–957 (2004).
36. S. E. Donnelly *et al.*, *Science* **296**, 507–510 (2002).
37. J. Hernández-Guzmán, E. R. Weeks, *Proc. Natl. Acad. Sci. U.S.A.* **106**, 15198–15202 (2009).

Acknowledgments: The raw data presented in this work are available in the supplementary movies. S.K. acquired, aligned, and preprocessed the TEM data under the supervision of U.K. P.Y.H. and J.S.A. designed and conducted the atom tracking and strain and deformation analysis under the supervision of D.A.M. and P.L.M. A.S., A.A.A., and J.P.S. contributed theoretical understanding via continuum mechanics analysis and LAMMPS simulations. P.Y.H., J.S.A, and D.A.M. wrote the paper. All authors contributed to the discussion of results and commented on and edited the paper. This work was supported by the NSF through the Cornell Center for Materials Research (NSF DMR-1120296). Additional support for P.Y.H. was provided by the NSF Graduate Research Fellowship Program under grant DGE-0707428. A.A.A., A.S., and J.P.S. were supported by NSF grant PHY-0941095. J.S.A. and P.L.M were supported by the Air Force Office of Scientific Research through the Graphene MURI (FA9550-09-1-0691 and FA9550-10-1-0410). U.K. and S.K. acknowledge support from the Deutsche Forschungsgemeinschaft (German Research Foundation) and the Ministry of Science, Research and the Arts (MWK) of Baden-Württemberg through the Sub Angstrom Low-Voltage Electron Microscopy project. The authors acknowledge discussions with M. K. Blees, I. Cohen, S. J. Gerbode, R. Hovden, J. Kotakoski, A. V. Krasheninnikov, B. Leahy, Y.-C. Lin, M. L. Manning, E. R. Weeks, and A. M. van der Zande. We thank A. Srivastava, V. Skakalova, and J. Smet from the Max Planck Institute for Solid State Research in Stuttgart, Germany, for the sample. Microscopy support and maintenance were provided by J. Biskupek.

Supplementary Materials
www.sciencemag.org/content/342/6155/224/suppl/DC1
Materials and Methods
Figs. S1 to S6
Movies S1 to S5
References (*38*–*40*)

21 June 2013; accepted 26 August 2013
10.1126/science.1242248

Waveform Tomography Reveals Channeled Flow at the Base of the Oceanic Asthenosphere

Scott French,[1] Vedran Lekic,[2] Barbara Romanowicz[1,3,4]*

Understanding the relationship between different scales of convection that drive plate motions and hotspot volcanism still eludes geophysicists. Using full-waveform seismic tomography, we imaged a pattern of horizontally elongated bands of low shear velocity, most prominent between 200 and 350 kilometers depth, which extends below the well-developed low-velocity zone. These quasi-periodic fingerlike structures of wavelength ~2000 kilometers align parallel to the direction of absolute plate motion for thousands of kilometers. Below 400 kilometers depth, velocity structure is organized into fewer, undulating but vertically coherent, low-velocity plumelike features, which appear rooted in the lower mantle. This suggests the presence of a dynamic interplay between plate-driven flow in the low-velocity zone and active influx of low-rigidity material from deep mantle sources deflected horizontally beneath the moving top boundary layer.

Mantle convection is responsible for driving plate motions on Earth, but the detailed morphology of convection patterns remains unresolved. Because seismic velocities are affected by temperature, and seismic anisotropy is affected by alignment of crystals, seismic tomography can be used to map the patterns of flow in the earth's mantle. Global seismic mantle tomography has provided important constraints on the long-wavelength shear-velocity structure, highlighting in particular the correlation of velocity patterns in the top 200 km with surface tectonics and documenting the widespread presence of the low-velocity zone (LVZ) under ocean basins. Likewise, the presence of two antipodal large low-shear-velocity provinces (LLSVPs) at the base of the mantle under the central Pacific and Africa is a robust feature of all tomographic models (*1*). Hotspots appear to be located preferentially above the LLSVPs (*2*) or on their borders (*3*). There is also a striking correlation at long wavelengths between the location of the LLSVPs and high attenuation in the mantle transition zone (*4*). However, plume conduits (*5*, *6*) and roll-like secondary convection patterns (*7*) remain difficult to image tomographically.

We used full-waveform inversion, coupled with synthetic seismogram computation using the Spectral Element Method, to image global radially anisotropic shear-velocity (V_S) structure at upper-mantle and transition-zone depths. This approach is well suited to remedy the known limitations of classical tomographic techniques (*8*), as already demonstrated at the local (*9*) and regional (*10*) scales. Our second-generation global model, SEMum2, refines an earlier one developed by our group (*11*) and in particular includes a more realistic crust (supplementary text and figs. S1 to S4). Compared with other global shear-velocity models (figs. S5 to S8), SEMum2 more accurately recovers both the depth and strength of the low-velocity minimum under ridges. It also shows stronger velocity minima in the LVZ, a more continuous signature of fast velocities in subduction zones, and stronger, clearly defined, low-velocity "conduits" under the Pacific Superswell (*12*) while confirming the robust long-wavelength structure imaged in previous studies (supplementary text S2.3 and figs. S7 and S8), such as the progressive weakening and deepening of the oceanic LVZ with overlying plate age.

Cluster analysis (*13*) of V_S profiles in the depth range 30 to 350 km in SEMum2 (supplementary text S3) provides an objective way to analyze the model and isolates an anomalously low-velocity region—most prominent in the depth range 200 to 350 km although also reflected in the overlying LVZ (Fig. 1, A and B, and fig. S9), organized in elongated bands, and clearest on the Pacific plate (Fig. 1A), where it spans from ~100 million-year-old ocean floor to the East Pacific Rise (EPR). In a map view of SEMum2 at a depth of 250 km (Fig. 2A), these prominent structures appear as fingerlike zones of significantly slower-than-average V_S (~3 to 4%). They are also present under other plates: off west Antarctica, in some parts of the North and South Atlantic and western Indian Oceans, and possibly in the southwestern part of the Australian plate (Fig. 2A and fig. S10). These fingerlike structures are not only well-resolved in the SEMum2 model but also are robust with respect to estimated model uncertainties, are compatible with independent waveform data, and cannot be explained by unmapped azimuthal anisotropy in our inversion (supplementary text S4 and figs. S13 to S17).

[1]Berkeley Seismological Laboratory, 209 McCone Hall, Berkeley, CA 94720, USA. [2]Department of Geology, University of Maryland, College Park, MD 20742, USA. [3]Collège de France, 11 Place Marcelin Berthelot, 75005 Paris, France. [4]Institut de Physique du Globe de Paris, 1 rue Jussieu, 752382 Paris Cedex 05, France.
*Corresponding author. E-mail: barbara@seismo.berkeley.edu

We find that these low-velocity fingers (LVFs) are oriented subparallel to the direction of absolute plate motion (APM) (Fig. 2B and supplementary text S5.1) (*14*). Perpendicular to the APM, the alternating zones of very low and somewhat higher-than-average V_S have a wavelength of ~2000 km, as illustrated in depth cross-sections on the Pacific Plate (Fig. 3, B and C). This wavelength corresponds to a peak in power in the geoid, as determined with directional wavelet analysis, which is also aligned with the direction of the APM (fig. S11 and supplementary text 5.3) (*15*). In cross-section parallel to the APM, the contrast in structure at depth within and adjacent to the LVFs is very clear (Fig. 3, D and E). The LVFs extend for many thousands of kilometers and reach beneath the conventional LVZ, which bottoms at an approximately constant depth of ~150 to 200 km (Fig. 3D). Below 200 km, velocities are as low within the LVFs as they are between fingers in the LVZ, despite the greater depth (Fig. 3). In contrast, the EPR itself is a shallow feature in isotropic V_S (fig. S6) but stands out in radial anisotropy as a zone where $V_{SV} > V_{SH}$ in the depth range 150 to 300 km (fig. S12C). This indicates that dominantly horizontal flow in the LVFs away from the ridge transitions to dominantly vertical flow under the ridge. Although local minima in the LVZ are associated with the LVFs, the strongest minima in the LVZ appear under ridges (Fig. 3 and fig. S12).

Such alternating zones of high and low velocities have previously been found along the Fiji-Hawaii corridor (*16*), and an elongate band of low velocities, within a similar depth range to the LVFs, has recently been imaged in the south Atlantic (*17*). At a smaller scale, tomographic maps based on the PLUME experiment (*18*, *19*) show a zone of fast velocities surrounding Hawaii, particularly strong in V_S to the southwest near 300 km depth. In our model, this corresponds to a domain of higher velocities between LVFs. Our study thus ties together these isolated observations, suggesting that they are manifestations of a single, consistent, large-scale pattern of LVFs (Figs. 2 and 3) aligned with the APM, present in the oceans worldwide, and extending in a narrow depth range below the LVZ.

At the global scale, many of the fingers underlie regions associated with hotspot tracks or seamount chains: for example, in the northwest Atlantic, the New England seamount chain, in the South Atlantic, the Walvis ridge, or the Cape Verde track, and in the Indian Ocean, portions of the Reunion hotspot track (Fig. 2 and fig. S10). In contrast to the top 300 km, deeper V_S structure in the region spanning from the Pacific Superswell to Hawaii is characterized by vertically elongated plumelike conduits (Fig. 4). Not all LVFs are connected to the conduits below, and the latter are not straight, but meander with depth and appear to be rooted in the lower mantle. The main hotspots in the central Pacific are located generally in the vicinity of the deep conduits but not immediately above them (Fig. 4D).

Although the resolution of our modeling enables the detection of the stronger mantle upwellings, such as those beneath Hawaii and the Superswell, the actual plume conduits could be narrower, and other, weaker ones, may not yet be resolved and will necessitate modeling at shorter periods (*6*). The absence of a direct vertical correspondence between hotspot locations and the imaged

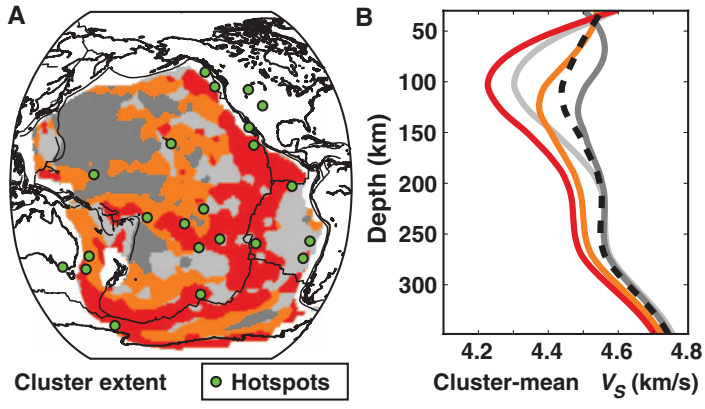

Fig. 1. Cluster analysis of oceanic upper-mantle shear velocity. (**A**) Pacific portion of a global cluster analysis (*13*) of model SEMum2 assuming four regions in the oceans (supplementary text S3). (**B**) Corresponding average depth profiles in each of the four regions (global average also shown, black dashed line).

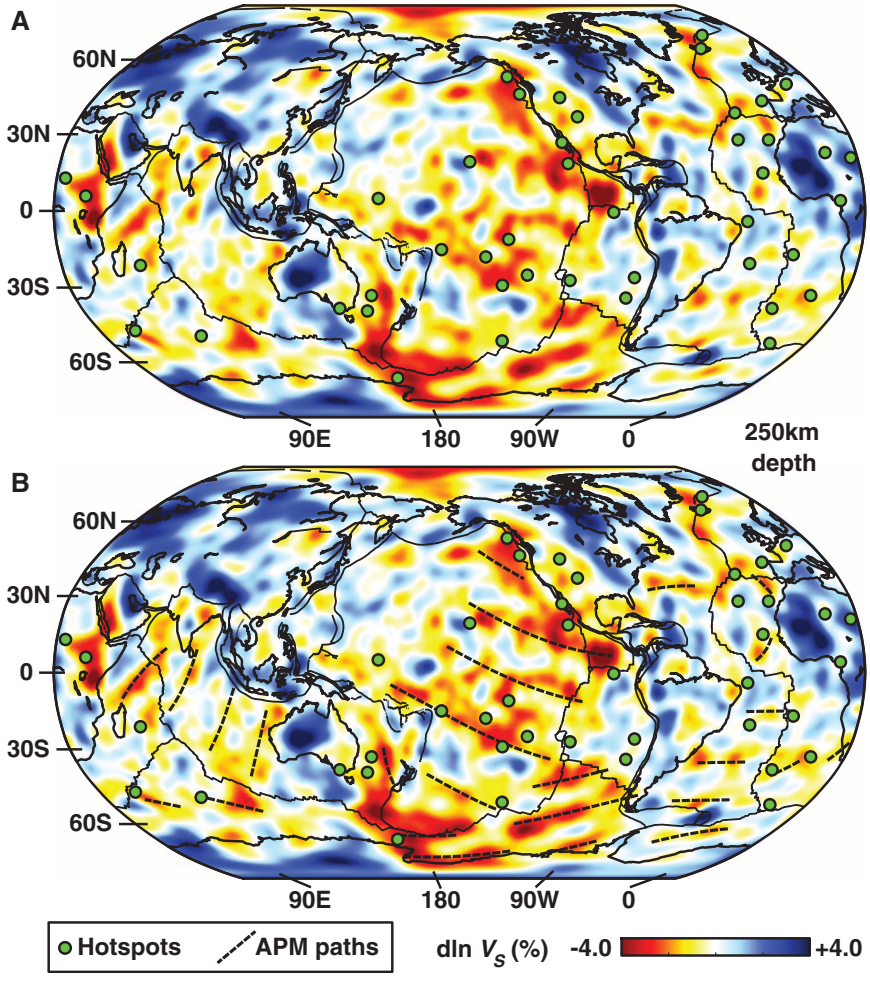

Fig. 2. Shear-velocity structure and absolute plate motion. (**A**) Map view of relative isotropic V_S variations (percent) from the mean at 250 km. (**B**) Identical to (A) but with plate-motion streamlines (broken lines) from the APM model of Kreemer (*14*). Green circles denote hotspot locations from Steinberger (*30*).

plumes suggests a complex interaction of the upwelling flow with the lithosphere (*20*). Above ~350 km depth, two interacting structural patterns appear to dominate: (i) the increasing depth and decreasing strength of the LVZ as a function of age in the depth range 50 to 200 km (Fig. 1B) and (ii) the difference in velocity—and therefore likely temperature and/or composition, as well as viscosity—within and outside of LVFs (Figs. 1B and 3 and supplementary text S5.2). In some locations, the LVFs appear to feed from the quasi-vertical conduits, suggesting deflection and channeling in the asthenosphere of active upwelling from low-viscosity plumes—similar to viscous fingering experiments in which a low-viscosity fluid is injected between two rigid horizontal plates or stratified, higher-viscosity fluids (*21*). This horizontally deflected flow then aligns in the direction of plate motion, driven by a combination of asthenospheric return flow (*22*, *23*) and upwelling-induced flow directed toward pressure minima at ridges (*24*–*26*). The pattern of radial anisotropy in the vicinity of the ridge (fig. S12C) further supports active ridge-ward flow in these channels. Active influx from deep upwellings deflected toward the ridge may be enhanced by flow in a narrow low-viscosity layer (*27*). The absence of any distinct deeper low-velocity structure beneath ridges (fig. S6), and the fact that some of the LVFs terminate at ridges (such as the Antarctic plate), confirms the passive nature of mantle upwelling beneath ridges.

Whether or not these observations can be explained by viscous fingering and channelization alone or in combination with other phenomena, such as secondary convection, is unknown. Other studies have described evidence for viscous fingering on the Pacific plate, aligned with the plate motion, albeit at an order-of-magnitude smaller spatial scale than seen here (*23*). The width of the fingers we observed (~1000 km) is large compared with the thickness of the channel (up to 350 km), whereas typical scaling in laboratory or numerical fingering experiments obtain a width-to-thickness ratio of ~2 (*21*). Secondary convection in the form of Richter rolls occurs with a horizontal-to-vertical scaling of 1 [albeit in a constant-viscosity fluid (*7*), a condition quite different from that in the Earth] but has previously been sought in the upper mantle at smaller scales than seen here (*28*). The LVFs are observed both below the fast spreading Pacific plate, where roll-like secondary convection may be expected, and below slow-moving plates [for example, the Antarctic plate (Fig. 2 and fig. S18) and the Atlantic Ocean (fig. S19)], where Richter rolls are unlikely to form. Comparison of the LVFs and Pacific geoid undulations with the same orientation and wavelength (fig. S11) (*15*) may also provide insight into causative dynamics. Indeed, in a simple Richter-like secondary convection scenario one would expect the bands of quasi-APM orientation in the geoid to be aligned vertically with the up- (LVF) and down-welling (inter-LVF) limbs. Instead, the LVFs fall at the edges or between these features—an observation more consistent with the presence of channelized flow (supplementary text S5.3). A further clue as to the nature and origin of the global pattern of LVFs that we document here might come from the geochemistry of mid-ocean ridge basalts, whose long-wavelength isotopic anomalies fluctuate with a similar pattern along the mid-Atlantic Ridge (*29*).

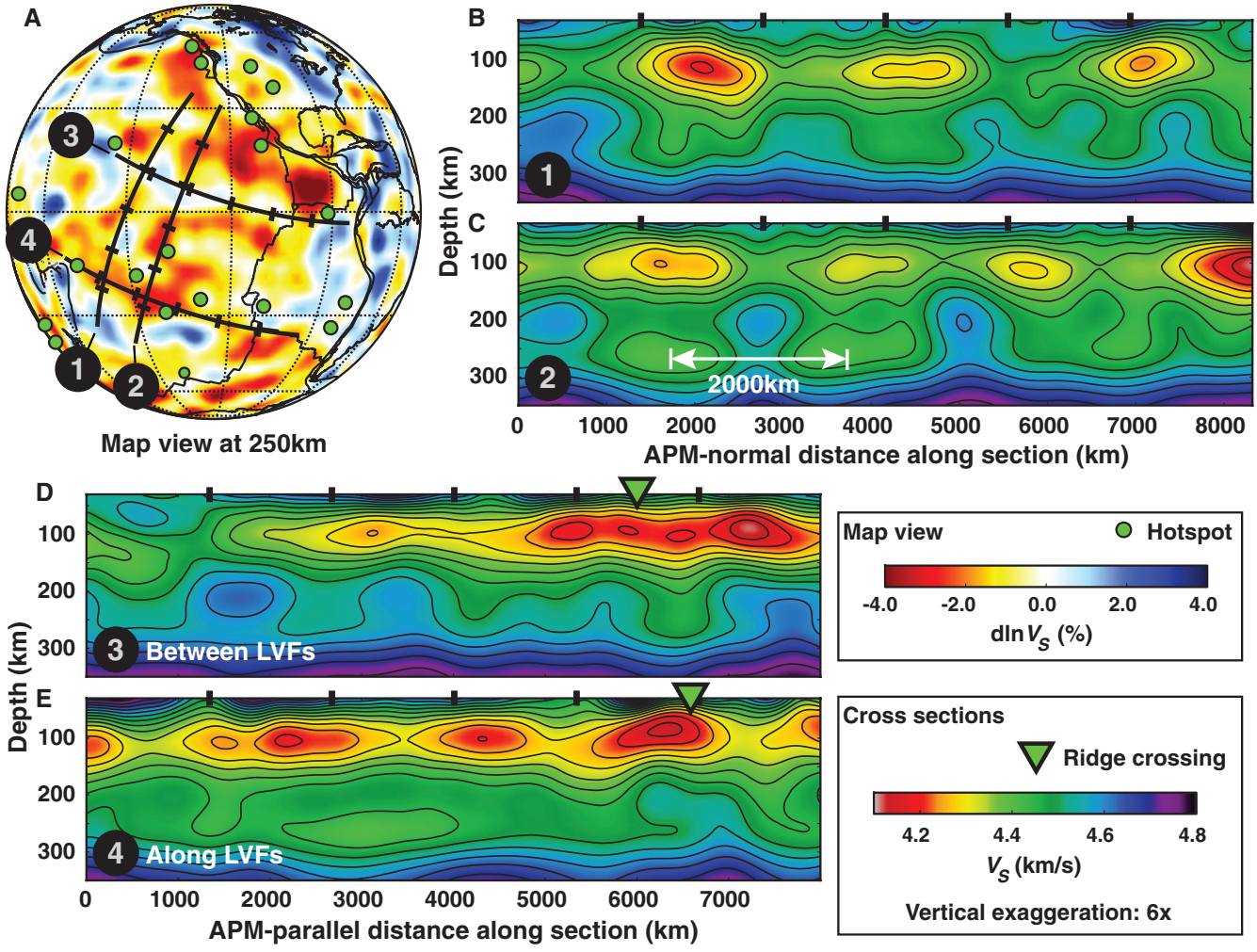

Fig. 3. Low-velocity fingers in cross-section. (**A**) Map view of relative isotropic V_S variations at 250 km depth, with location of depth profiles shown in (B) to (E). (**B** and **C**) Absolute variations in isotropic V_S along two profiles perpendicular to the APM. (**D** and **E**) Same as (B) and (C) for profiles parallel to the APM: (D) between two LVFs and (E) along an LVF. Green circles in (A) denote hotspots of Steinberger (*30*).

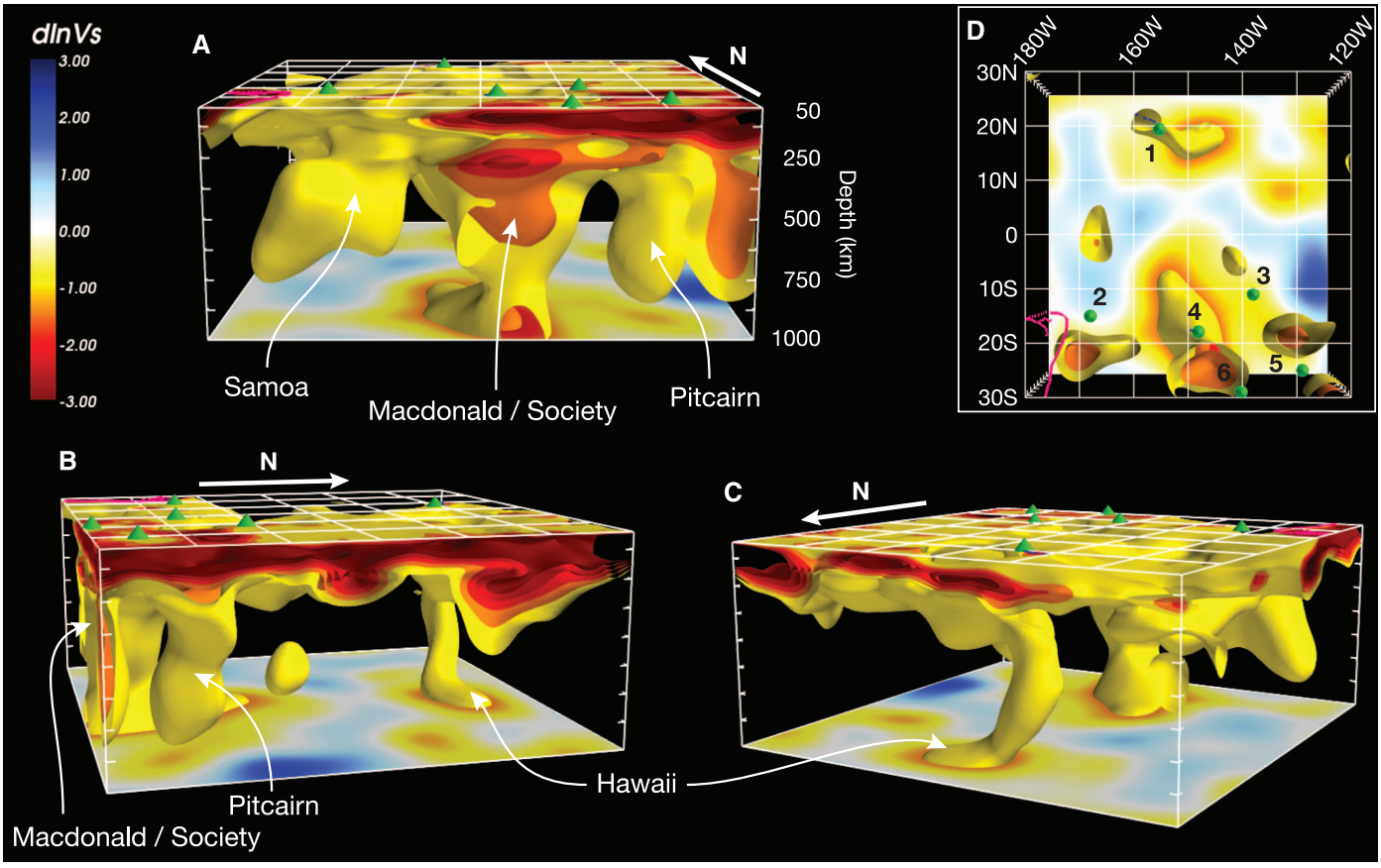

Fig. 4. Three-dimensional rendering of SEMum2 shear-velocity structure. Isotropic relative V_S variations in the central Pacific region (from the Superswell north to Hawaii) viewed from (**A**) the south, (**B**) the east and (**C**) the north. Minimum and maximum isosurface levels are −3 and −1%, respectively. In (A), the LVZ becomes thinner to the west, and the LVF disappears at the Tonga-Fiji subduction zone. In (B), the LVFs appear clearly separated from one another in the direction perpendicular to the APM. The absence of pronounced horizontally elongated low velocities below 200 km depth between fingers is visible in (C). Below 300 to 400 km, the low velocities are organized into predominantly vertical plume-like features. In particular, the Hawaiian "plume" appears east of Hawaii at the bottom of our model (1000 km depth) then turns to the northwest, before being deflected eastward again just below the LVF [(B) and (C)]. (**D**) View from the top shows the geographic location of the box and major hotspots in relation to the low-velocity conduits, rendered here at 500 km depth: 1, Hawaii; 2, Samoa; 3, Marquesas; 4, Tahiti 5, Pitcairn; and 6, Macdonald. The magenta outline indicates the location of the Tonga-Fiji subduction zone. Hotspot locations are those of Steinberger (*30*).

References and Notes

1. V. Lekic, S. Cottaar, A. M. Dziewonski, B. Romanowicz, *Earth Planet. Sci. Lett.* **357–358**, 68–77 (2012).
2. M. Richards, D. Engebretson, *Nature* **355**, 437–440 (1992).
3. A. Davaille, E. Stutzmann, G. Silveira, J. Besse, V. Courtillot, *Earth Planet. Sci. Lett.* **239**, 233–252 (2005).
4. B. Romanowicz, Y. C. Gung, *Science* **296**, 513–516 (2002).
5. W. J. Morgan, *Nature* **230**, 42–43 (1971).
6. F. Rickers, A. Fichtner, J. Trampert, *Geophys. J. Int.* **190**, 650–664 (2012).
7. F. M. Richter, B. Parsons, *J. Geophys. Res.* **80**, 2529–2541 (1975).
8. G. Nolet, F. A. Dahlen, *J. Geophys. Res.* **105**, (B8), 19043–19054 (2000).
9. C. Tape, Q. Liu, A. Maggi, J. Tromp, *Science* **325**, 988–992 (2009).
10. A. Fichtner, B. L. N. Kennett, H. Igel, H.-P. Bunge, *Geophys. J. Int.* **179**, 1703–1725 (2009).
11. V. Lekić, B. Romanowicz, *Geophys. J. Int.* **185**, 799–831 (2011a).
12. M. K. McNutt, K. M. Fischer, in *Seamounts, Islands and Atolls, Geophysical Monographs Series 43*, B. H. Keating *et al.*, Eds. (AGU, Washington D. C., 1987), pp. 25–34.
13. V. Lekic, B. Romanowicz, *Earth Planet. Sci. Lett.* **308**, 151–160 (2011b).
14. C. Kreemer, *J. Geophys. Res.* **114**, B10405 (2009).
15. M. Hayn *et al.*, *Geophys. J. Int.* **189**, 1430–1456 (2012).
16. R. Katzman, L. Zhao, T. H. Jordan, *J. Geophys. Res.* **103**, 17933–17971 (1998).
17. L. Colli, A. Fichtner, H.-P. Bunge, *Tectonophysics*, published online 27 June 2013 (10.1016/j.tecto.2013.06.015).
18. C. J. Wolfe *et al.*, *Earth Planet. Sci. Lett.* **303**, 267–280 (2011).
19. G. Laske *et al.*, *Geophys. J. Int.* **187**, 1725–1742 (2011).
20. J. M. O'Connor *et al.*, *Nat. Geosci.* **5**, 735–738 (2012).
21. D. Snyder, S. Tait, *J. Fluid Mech.* **369**, 1–21 (1998).
22. J. Phipps Morgan, W. J. Morgan, Y.-S. Zhang, W. H. F. Smith, *J. Geophys. Res.* **100**, (B7), 12,753–12,767 (1995).
23. N. Harmon, D. W. Forsyth, D. S. Weeraratne, Y. Yang, S. C. Webb, *Earth Planet. Sci. Lett.* **311**, 306–315 (2011).
24. D. R. Toomey *et al.*, *Earth Planet. Sci. Lett.* **200**, 287–295 (2002).
25. J. K. Hillier, A. B. Watts, *J. Geophys. Res.* **109**, B10102 (2004).
26. M. D. Ballmer, C. P. Conrad, E. I. Smith, N. Harmon, *Geology* **41**, 479–482 (2013).
27. T. Höink, A. Lenardic, M. Richards, *Geophys. J. Int.* **191**, 30–41 (2012).
28. M. D. Ballmer, J. van Hunen, G. Ito, T. A. Bianco, P. J. Tackley, *Geochem. Geophys. Geosyst.* **10**, GC002386 (2009).
29. A. W. Hofmann, in *Treatise on Geochemistry Update 1*, H. D. Holland, K. K. Turekian, Eds. (Elsevier, New York, 2007), vol. 2.03, pp. 1–44.
30. B. Steinberger, *J. Geophys. Res.* **105**, 11,127–11,152 (2000).

Acknowledgments: We thank A. Davaille, C. Jaupart, and D. Shim for helpful discussions. This work was supported by the National Science Foundation (NSF) (grant EAR-0738284). S.F. acknowledges support from a NSF Graduate Research Fellowship. Our waveform data set was collected from the Incorporated Research Institutions for Seismology (www.iris.edu). Computations were performed at the National Energy Research Scientific Computing Center (supported by the U.S. Department of Energy Office of Science, contract DE-AC02-05CH11231). This is Berkeley Seismological Laboratory contribution 13-13. The SEMum2 model is available at http://seismo.berkeley.edu/~sfrench/SEMum2.

Supplementary Materials

www.sciencemag.org/content/342/6155/227/suppl/DC1
Supplementary Text
Figs. S1 to S19
Table S1
References (*31–60*)

17 April 2013; accepted 26 August 2013
Published online 5 September 2013;
10.1126/science.1241514